

See discussions, stats, and author profiles for this publication at: <http://www.researchgate.net/publication/255760568>

One-pot synthesis of hexagonal and triangular nickel-copper alloy nanoplates and their magnetic and catalytic properties

ARTICLE *in* JOURNAL OF MATERIALS CHEMISTRY · APRIL 2012

Impact Factor: 7.44 · DOI: 10.1039/C2JM16095A

CITATIONS

18

READS

81

5 AUTHORS, INCLUDING:



[Huizhang Guo](#)

ETH Zurich

30 PUBLICATIONS 252 CITATIONS

[SEE PROFILE](#)



[Dong-Liang Peng](#)

Xiamen University

167 PUBLICATIONS 1,656 CITATIONS

[SEE PROFILE](#)

One-pot synthesis of hexagonal and triangular nickel–copper alloy nanoplates and their magnetic and catalytic properties†

Huizhang Guo, Yuanzhi Chen,* Hemei Ping, Laisen Wang and Dong-Liang Peng*

Received 23rd November 2011, Accepted 22nd February 2012

DOI: 10.1039/c2jm16095a

A facile one-pot route has been developed for the synthesis of hexagonal and triangular Ni–Cu alloy nanoplates. The synthesis was conducted using nickel(II) acetylacetonate and copper(II) chloride dihydrate as metal precursors, trioctylphosphine as a capping agent, and oleylamine as a solvent and reducing agent. Structural analyses from X-ray diffraction and transmission electron microscopy indicate that the as-synthesized nanoplates have an fcc crystalline structure and their side faces are bound by a mixture of {100} and {111} facets, while their top and bottom faces are bound by {111} facets. The oxidative etching effect of Cu(II) on Ni(0) in the presence of Cl ions plays an important role in the generation of the anisotropic nanoplates. The results of magnetic measurements revealed differences between the hexagonal and triangular nanoplates in their ability to undergo the transition from the ferromagnetic to the superparamagnetic state with increasing temperature. The magnetic properties of the as-synthesized Ni–Cu alloy nanoplates can also be tuned by adjusting the Ni content which correlates closely with reaction temperature. Excellent catalytic properties for the catalytic reduction of methylene blue by NaBH₄ in aqueous solution were observed for the as-synthesized nanoplates.

Introduction

The composition-dependent shape-anisotropy and the surface structure of bimetallic nanocrystals (NCs) have been attracting an increasing amount of attention.^{1–3} The shape-controlled synthesis of metal NCs is meaningful as it enables scientists to tailor a variety of properties such as the catalytic activity and selectivity which depend closely on exposed facets. For example, Yan *et al.* demonstrated that {100}-facet-enclosed Pt–Pd nanocubes had higher electrocatalytic activity, while {111}-facet-enclosed Pt–Pd nanotetrahedrons exhibited a better durability.⁴ At the same time, atoms that are located at the exposed edges and corners also have profound effects on a NC's properties, especially its catalytic performance. Introduction of twin defects into NCs, which can break the cubic symmetry of the face-centered cubic (fcc) metal lattices, is essential to obtain an anisotropic structure such as nanoplates. The twin defects in NCs result in a large defect-to-volume ratio in nanoplates, which may contribute to the properties that are substantially different from those of their single-crystal counterparts. Twinning boundaries which exist within the metal NCs can serve as atom transport

channels which form an additional diffusion network within twin NCs and promote the inward and outward flow of atoms.⁵

As the shape of metal NCs may greatly affect their properties and performances for a given application, it is vital for scientists to master the synthetic strategies and understand the formation mechanism behind them. Over the past decade, there has been a large number of reports on the successful synthesis of noble metal NCs in a variety of shapes, such as Ag cuboctahedrons,⁶ triangular and hexagonal Pd nanoplates,⁷ Pt nanocubes,⁸ and Au octahedrons.⁹ However, since the magnetic transition metals have a greater negative potential than the noble metals, the preparation of magnetic transition metal NCs with shape-anisotropy is still a significant challenge. In contrast to numerous reports on the preparation of shape-anisotropic noble metal NCs, there are limited reports on the successful preparation of magnetic NCs with shape-anisotropy. Metal carbonyl pyrolysis is an established method to obtain anisotropic magnetic NCs. For example, Co nanodisks and nanorods were synthesized using Co₂(CO)₈ as a precursor.¹⁰ Fe(CO)₅ was used to generate Fe species that could promote the formation of Ni nanoplates/nanodisks.^{11,12} The major problem associated with using metal carbonyl compounds is that most of them are highly toxic and are not environmentally friendly for practical production. Co and Ni nanoplatelets were also prepared in an autoclave using a hydrothermal method.¹³ Overall, reports on the synthesis of magnetic metal nanoplates using conventional chemical solution methods are rather rare.

On the other hand, the different atomic segregation behaviour and the synergy between the two metals in bimetallic NCs usually

Department of Materials Science and Engineering, College of Materials, Xiamen University, Xiamen, 361005, P. R. China. E-mail: yuanzhi@xmu.edu.cn; dlpeng@xmu.edu.cn; Fax: +86 592 2183515; Tel: +86 592 2180155

† Electronic supplementary information (ESI) available: TEM images, elemental maps, XRD patterns, magnetic property data and synthetic method details for the different samples. See DOI: 10.1039/c2jm16095a

bring enhanced or new properties.^{2,14,15} Bimetallic NCs are expected to have excellent performances which can be exploited in various fields such as biotechnology,¹⁶ magnetic recording¹⁷ and catalysis.¹⁸ However, when more than one metal precursor is used to synthesize bimetallic NCs, the formation mechanism becomes complex because the reaction is greatly affected by the chemical nature of each metal precursor. Recently, a couple of synthetic approaches such as the bimetallic-compound thermal-decomposition route,¹⁹ seeded-growth process,² and noble-metal-induced-reduction strategy^{20–22} have been used to obtain bimetallic NCs without separate monometallic phases. However, the synthesis of bimetallic NCs with high shape-anisotropy is not only a thermodynamically controlled process, but also a kinetically controlled one. Therefore, every synthetic parameter including the metal precursor, reducing agent, capping agent and aging temperature should be selected carefully.

Herein we report the synthesis of hexagonal and triangular Ni–Cu alloy nanoplates with a well-defined twin structure using a facile one-pot non-aqueous synthetic approach. To the best of our knowledge, non-aqueous syntheses of Ni–Cu alloy nanoplates have not yet been reported. Unlike many reported studies in which toxic metal carbonyl compounds were used to obtain anisotropic structures, we employed common reagents, *i.e.* copper(II) chloride dihydrate and nickel(II) acetylacetonate, as metal precursors. Interestingly, copper chloride not only acted as a metal precursor, but also introduced Cu²⁺ and Cl[−] into the solution to control the growth speed of the NCs by oxidizing Ni(0) back to Ni(II) during a galvanic replacement reaction process. We also demonstrate that the shape of the NCs can change from hexagonal to triangular at different synthetic conditions. Finally the magnetic and catalytic properties of the as-prepared Ni–Cu alloy nanoplates are reported.

Experimental section

Materials

Oleylamine (80–90%) and dibenzyl ether (95%) were purchased from Acros Organics. Nickel(II) acetylacetonate (Ni(acac)₂, 96%) and trioctylphosphine (TOP, 97%) were purchased from Strem Chemical Inc. Copper(II) chloride dihydrate (CuCl₂·2H₂O), sodium borohydride (NaBH₄), ethyl alcohol, acetone, hexane and toluene were all chemically pure and purchased from SCRC. Methylene blue trihydrate (98.5%) was purchased from Xilong Chemical Inc. All of the chemicals were used as received.

Synthesis of hexagonal Ni–Cu alloy nanoplates

In a typical synthesis, a mixture of 7 mL of oleylamine, 1 mmol of Ni(acac)₂, 0.2 mmol of CuCl₂·2H₂O was decanted into a three-necked flask and kept under a flow of high-purity argon gas at 110 °C for 20 min with strong magnetic stirring before 1 mmol of TOP was injected. After stirring for 5 min, the resulting solution was then slowly heated up to 220 °C (reaction temperature can range from 175 °C to 240 °C) and aged at this temperature for 60 min. After cooling down to room temperature naturally, excess acetone was added to the black solution to give a black precipitate which was isolated *via* centrifugation (6500 rpm for 3 min). The precipitate was then washed fully with a mixture of hexane and acetone, and dried in a vacuum drying oven at 50 °C

for one hour to obtain a dry powder. A portion of the powder was dispersed in hexane *via* ultrasound concussion in an ultrasonic wave apparatus for 15 min for characterization purposes.

Synthesis of triangular Ni–Cu alloy nanoplates

A mixture of 7 mL of oleylamine, 3 ml of dibenzyl ether, 1 mmol of Ni(acac)₂, and 0.2 mmol of CuCl₂·2H₂O was decanted into a three-necked flask, and kept under a flow of high-purity argon gas at 110 °C for 20 min with strong magnetic stirring before 1 mmol of TOP was injected. After stirring for 5 min, the resulting solution was then slowly heated up to 200 °C and aged at this temperature for 60 min. The remaining steps are the same as those for the synthesis of hexagonal nanoplates.

Characterization

X-Ray diffraction (XRD) patterns were recorded using a Panalytical X³pert PRO X-ray diffractometer with Cu K_α radiation. Transmission electron microscopy (TEM) images, energy dispersive X-ray spectroscopy (EDS) data, and electron diffraction data were collected on a JEM-2100 transmission electron microscope operating at 200 kV. Elemental maps were acquired on a TECNAI F-30 transmission electron microscope equipped with a scanning TEM (STEM) unit and a high-angle annular dark-field (HAADF) detector. The TEM samples were prepared by dropping the particle suspensions in toluene onto a gold grid coated with carbon film before drying at room temperature under ambient conditions. Magnetic measurements were carried out with a superconducting quantum interference device magnetometer (SQUID, MPMS-5) in a temperature range of 5–375 K. During zero-field-cooled (ZFC) and field-cooled (FC) measurements, the measuring and cooling fields were 100 Oe. The maximum value of the applied magnetic field during the hysteresis loop measurements was 50 kOe. UV-visible spectroscopic data were obtained on a Shimadzu UV-2550 ultraviolet visible spectrophotometer.

Catalysis test

To study the catalytic properties of the as-synthesized alloy nanoplates, we evaluated their catalytic activities for the catalytic reduction of methylene blue by NaBH₄ in water. In a typical experiment, 10 mL of methylene blue aqueous solution (50 mg L^{−1}) was added into a glass beaker which contained 5 mg of catalyst. After 5 min of sonic oscillation, the glass beaker was kept in a thermostat with magnetic stirring at 25 ± 1 °C. 10 mL of NaBH₄ aqueous solution (2.7 g L^{−1}) was then added to this reaction mixture as a sudden supply through a syringe. UV-vis absorption spectroscopy was used to monitor the discolorization process of the mixture. For the purpose of comparison, metallic Ni and Cu nanoparticles were also chosen for testing.

Results and discussion

Structural and compositional characterization

Fig. 1a displays a representative TEM image of the products obtained from the typical synthesis of hexagonal Ni–Cu alloy nanoplates. The product consists of hexagonal nanoplates with

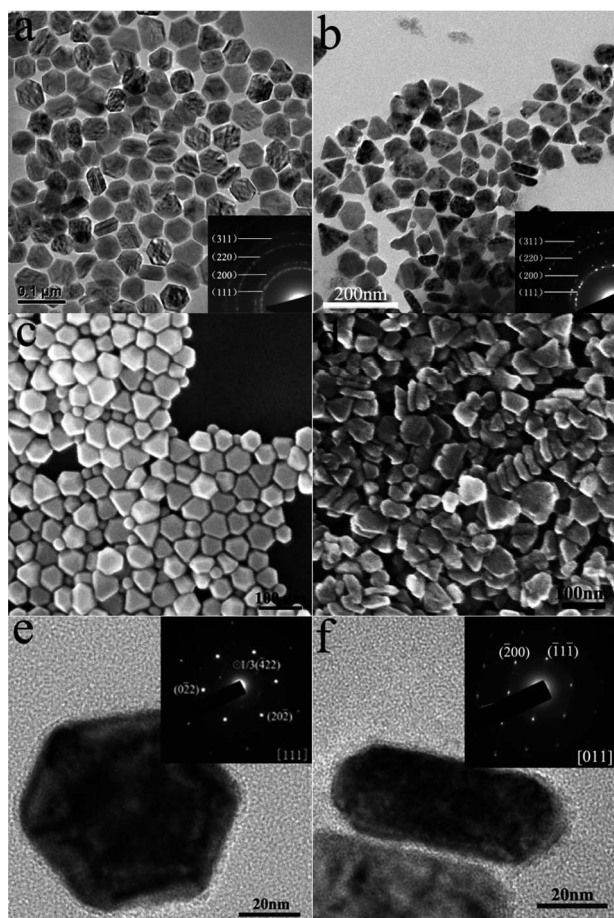


Fig. 1 (a) and (b) are the TEM images along with corresponding SAED patterns (inserts) of the as-synthesized hexagonal and triangular Ni–Cu alloy nanoplates, respectively. (c) and (d) are the SEM images of the as-synthesized hexagonal and triangular Ni–Cu alloy nanoplates, respectively. (e) and (f) are the top-face and side-face TEM images along with corresponding SAED patterns (inset) of a hexagonal nanoplate, respectively.

an average edge length of 31 ± 4.5 nm (see Fig. S1 in ESI† for more detailed information on size distribution) as well as a few (about 10%) NCs with other shapes. The TEM image also displays some rod-like shapes which are caused from the lateral orientation of the nanoplates relative to the electron beam. This lateral orientation directly exposes the side profile of the nanoplates. The determined nanoplate thickness is 26 ± 4.0 nm. Once oleylamine was diluted by dibenzyl ether to a molar ratio of 3 to 7 (oleylamine to dibenzyl ether) along with the decrease of reaction temperature down to 200 °C, the shape of the Ni–Cu alloy nanoplates converts from hexagonal to triangular.

Fig. 1b shows a TEM image of the products obtained from the typical synthesis of triangular Ni–Cu alloy nanoplates. Triangular nanoplates that have an average edge length of 71 ± 9.4 nm (see Fig. S2 in ESI† for more detailed information on size distribution) and a thickness of 21 ± 3.4 nm constitute the main body. In addition, NCs (about 30%) with other shapes are also observed. The nanoplate morphology can be easily verified from the SEM images (Fig. 1c and 1d). Selected area electron diffraction (SAED) patterns recorded from both the hexagonal

and triangular nanoplates (the inserts in Fig. 1a and 1b) exhibit multiple diffraction rings, which is consistent with an fcc structure of a Ni–Cu alloy. The XRD analysis result also agrees well with that of the SAED analyses. In the XRD patterns (see Fig. S3 in ESI†), three major characteristic diffraction peaks ((111), (200) and (220)) do not match well with those of fcc Ni or fcc Cu, instead the positions of these peaks are between those of fcc Ni and fcc Cu, indicating that an alloy structure has formed.

To further characterize the structure of the as-prepared nanoplates, SAED patterns were collected on individual nanoplates. Fig. 1e shows the SAED pattern of a hexagonal nanoplate with its hexagonal flat face perpendicular to electron beam. The obtained SAED pattern can be indexed to the [111] zone axis of the fcc Ni–Cu alloy, which indicates that the flat face is the (111) facet. Besides the six bright diffraction spots in a 6-fold symmetry corresponding to $\{220\}$ facets, the forbidden $1/3\{422\}$ diffraction spots with a much weaker intensity could also be observed in the SAED pattern. Usually the $1/3\{422\}$ diffraction spots cannot be observed in crystals with a perfect fcc structure. The reasons for the occurrence of these forbidden diffraction spots are complex. Defect structures such as twins and stacking faults may account for their presence. Similar diffraction spots were also observed by many authors in NCs of Ag,^{23–27} Au,^{23,28} Au@Cu²⁹ and Au@Ni.³⁰ A couple of models^{23–26} have been proposed for the explanation of the observed forbidden diffraction spots, such as the stacking fault model,^{24,25} and the twin boundary model.²³ Fig. 1f shows a TEM image of a hexagonal nanoplate in the side view. The corresponding SAED pattern is indexed to the [011] zone axis. These data clearly confirm that the as-synthesized nanoplates have a plate-like structure.

TEM images of the nanoplates from different orientations indicate a morphology that consists of two regular triangles/hexagons placed base-to-base, with a twinning plane bisecting the entire structure. To obtain the information on side faces, tilting experiments were conducted on individual nanoplates. The diffraction patterns obtained from most of the flat hexagonal nanoplates without tilting the sample stage are characteristic of the [111] zone axis (Fig. 2a middle), indicating that the nanoplate is bound by two $\{111\}$ facets on the top and bottom faces and by one $\{111\}$ facet in contact with the substrate. When the hexagonal nanoplate was tilted by 34.8° , the SAED pattern taken along the [011] zone axis was observed. Since $\{200\}$ diffraction spots which correspond to the side-edge used as the tilting axis appear in the SAED pattern and the angle between the (011) and (100) facets is 90° , the corresponding side facet should be a $\{100\}$ facet. When the hexagonal nanoplate was tilted off the [111] zone axis by 19.5° along another side-edge, the diffraction spot from the (111) facet which has an angle of 90° to the (112) facet appears in the SAED pattern viewed in the [112] zone axis, indicating that the side-edge should be a $\{111\}$ facet. On the basis of these diffraction patterns and symmetry considerations, we can deduce that the side facets of a hexagonal nanoplate must be bound by $\{100\}$ and $\{111\}$ facets placed alternatively. Such a structural configuration is similar to that of fcc noble metal nanodisks/nanoplates discussed by Wang³¹ and Xia⁷ *et al.* For the triangular nanoplate (Fig. 2b), when the crystal was tilted off the [111] zone axis by 35.5° , a SAED pattern in the [011] zone axis was obtained. Similar to the case discussed in Fig. 2a, this SAED pattern confirms that the side facets of

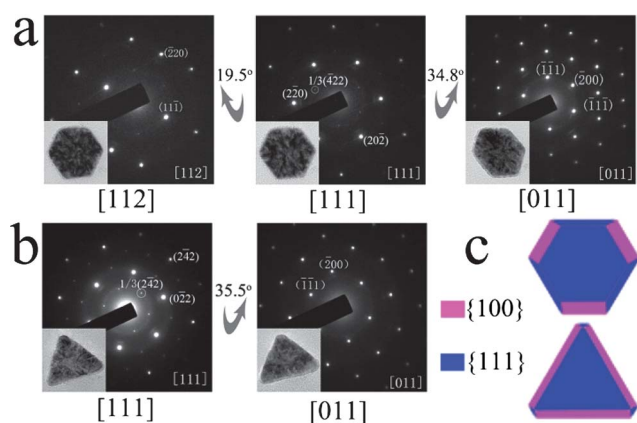


Fig. 2 (a) SAED patterns of a single hexagonal Ni–Cu alloy nanoplate viewed along the [112], [111] and [011] zone axes. (b) SAED pattern of a single triangular Ni–Cu alloy nanoplate viewed along the [111] and [011] zone axes. The tilted angles among different zone axes during observation are indicated. The inset of each figure shows the TEM image of the nanoplate at corresponding zone axis. (c) Schematic drawing of the hexagonal and triangular nanoplates. The {111} and {100} facets are represented using different colours.

a triangular nanoplate are bound by {100} facets, which is in accordance with the Pd nanoplates discussed by Xia⁷ and the truncated bipyramids of Ag discussed by Mirkin.³² The proposed structure models for hexagonal and triangular Ni–Cu alloy nanoplates are illustrated in Fig. 2c.

The EDS spectra recorded from individual triangular and hexagonal nanoplates undoubtedly show the presence of both Ni and Cu (see Fig. S4 in ESI†). To further study the distribution of Ni and Cu in the nanoplate, a HAADF image (Fig. 3a) of a triangular nanoplate along with its STEM-EDS line-scanning profile (Fig. 3b) and STEM-EDS elemental maps (Fig. 3c and 3d) were recorded. The results show that both Cu and Ni are distributed throughout the whole nanoplate, indicating an alloy structure. However, this distribution is not totally even and Cu seems to concentrate more in the nanoplate center than at the edge (see the line-scanning profile). STEM-EDS mapping conducted on a single hexagonal nanoplate (see Fig. S5 in ESI†) also revealed a similar result on the distribution of Ni and Cu in the nanoplate. The observed result is related to the formation mechanism which will be discussed later. Since the NCs formed at the beginning stage are rich in Cu, and the content of Ni increases later as the reaction time increases, complete homogenization of Cu and Ni may not be easily achieved within a limited reaction time. More aging time or higher aging temperatures are needed to achieve an equal distribution of Ni and Cu *via* atomic diffusion throughout the nanoplate.

Formation mechanism

The facile synthesis was conducted in oleylamine which served as a solvent, surfactant and reducing agent. Dibenzyl ether was used to dilute the reducing agent, thereby controlling the reaction kinetics. What is worth noting first is that the shape of the Ni–Cu bimetallic NCs is concerned with different Cu precursor compounds. When copper acetate monohydrate was used rather than $\text{CuCl}_2 \cdot 2\text{H}_2\text{O}$, only spherical Ni–Cu alloy nanoparticles were

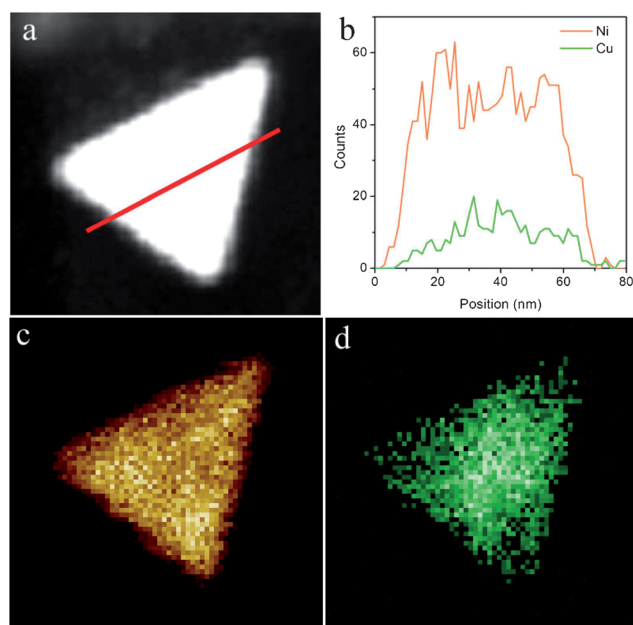


Fig. 3 HAADF image (a), STEM-EDS line-scanning profile (b) taken along the red line in image (a), and STEM-EDS elemental maps ((c) for Ni and (d) for Cu) of a single triangular Ni–Cu alloy nanoplate that was synthesized using the typical synthesis described in experimental section.

formed (see Fig. S6–S8 in ESI†). Meanwhile, if copper dinitrate trihydrate was applied in this reaction system, mixed NCs of Cu and NiO could be generated (see Fig. S9 and S10 in ESI†). Interestingly, when $\text{CuCl}_2 \cdot 2\text{H}_2\text{O}$ was applied, anisotropic Ni–Cu alloy NCs were obtained. We need to point out that no products will be obtained even at a temperature of 300 °C, if we only use $\text{CuCl}_2 \cdot 2\text{H}_2\text{O}$ as a single Cu salt precursor without any $\text{Ni}(\text{acac})_2$ in oleylamine solution. At the same time, according to our former study, Ni nanoparticles could not be formed at a temperature below 175 °C in oleylamine.³³ However, when a slight amount of $\text{CuCl}_2 \cdot 2\text{H}_2\text{O}$ was added, Ni–Cu alloy nanoparticles could be acquired at a relatively low temperature (170 °C). This is because Cu atoms can be produced on the surface of Ni crystal embryos by the galvanic replacement reaction between Ni atoms and $\text{Cu}(\text{II})$ ions, since the redox pair potential of Ni^{2+}/Ni (−0.246 V) is smaller than that of Cu^{2+}/Cu (0.337 V). Then the generated Cu atoms may further catalyze the reduction of Ni ions. Similar galvanic replacement reactions have also been noticed in other metal systems, such as Co/Au,³⁴ Pd/Pt³⁵ and Ag/Au.³⁶ After the deposition of Cu atoms on the surface of the Ni crystal embryos, the electrons can transfer to Ni ions from the surface Cu atoms much easier than from solution, which enables the growth of a Ni–Cu bimetallic crystal embryo at a temperature lower than the growth threshold of a pure Ni nucleus.

The control experiment with KCl (providing Cl ions) instead of $\text{CuCl}_2 \cdot 2\text{H}_2\text{O}$ led to the generation of spherical Ni nanoparticles (see Fig. S11 in ESI†). This indicates that both Cl ions and Cu ions play an irreplaceable role in the production of anisotropic Ni–Cu alloy nanoplates. Cl ions can restrain Cu ions from being reduced by oleylamine so that Cu ions can only be turned into zero-valent Cu through galvanic replacement reactions between Cu ions and Ni. The galvanic replacement

reactions between Cu ions and Ni slow the nucleation and growth enough for it to be under kinetic control, and result in a final product with high anisotropy. Therefore, $\text{CuCl}_2 \cdot 2\text{H}_2\text{O}$ is not only one of the reactants, but also an important surface etching agent for the generation of nanoplates.

In order to obtain further information on the formation of Ni–Cu nanoplates, the products generated at different reaction stages in the typical synthesis of hexagonal nanoplates were collected for TEM characterization. As shown in Fig. 4a, Ni–Cu nanoclusters with a scale of about 2.5 nm can be observed when the reaction was ceased immediately once the temperature reached 200 °C. The nanoclusters contained about 6.2% atomic percent of Ni which was indicated from EDS analysis (see Fig. S12 in ESI†). The low content of Ni could be ascribed to the reason that most of the Ni(0) was etched back to solution by Cu ions. Then, these clusters grew into monodisperse spherical NCs with a diameter of 20 nm after slowly being heated to 210 °C (Fig. 4b). After aging at this temperature for 15 min, these spherical NCs transformed into bigger ones having a diameter of about 27 nm and a slight shape-anisotropy (Fig. 4c). Many of the NCs contained crystalline defects which are vital for the formation of nanoplates. From the EDS analysis, the content of Ni increased from 39.4% to 77.9% (see Table S1 in ESI†) when the reaction time was prolonged to 30 min. Finally, almost all of the NCs converted into hexagonal nanoplates after aging at 210 °C for 30 min (Fig. 4d).

Based on the above results and discussions, a possible formation mechanism of Ni–Cu alloy nanoplates is proposed (Scheme 1). At first, Ni(II) is reduced into zero-valent atoms which then combine into crystal embryos that are smaller than

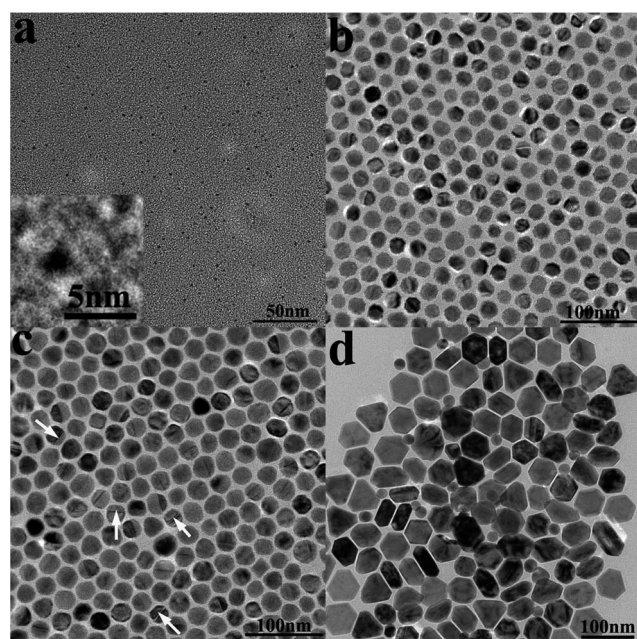
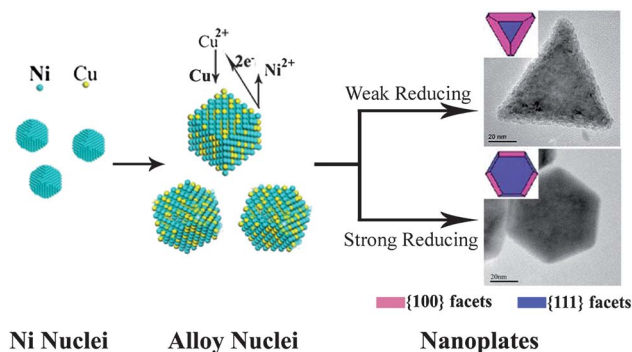


Fig. 4 TEM images of the products obtained at different reaction stages in the typical synthesis of Ni–Cu hexagonal nanoplates: (a) 200 °C, 0 min (inset shows the enlarged image); (b) 210 °C, 0 min; (c) 210 °C, 15 min (crystalline defects are indicated by white arrows); (d) 210 °C, 30 min. More information about the synthetic conditions is available in Table S1 (see No. 10–13) in ESI†.

their critical nucleation size (the size of a stable nucleus that can grow spontaneously in the supersaturated solution). After that, Cu(II) which cannot easily be reduced by oleylamine in the presence of Cl ions will etch the surface Ni(0) partially back to the solution during galvanic replacement reactions. The zero-valent Cu deposited on the surface of the Ni embryos will further catalyze the reduction of Ni(II) to form alloy nuclei. Then reiteration of this oxidative etching and catalytic growth process, together with the inclusion of crystalline defects (e.g. stacking faults and twins) enable the alloy nuclei to grow to spherical seeds that finally develop into alloy nanoplates whose final shapes are determined by the competition of the reduction rate of Ni(II) and the etch rate of Ni(0). A relatively strong reducing environment preferably generates hexagonal nanoplates.

Influence of temperature

It should be noted that there is a direct link between the reaction temperature and the shape of the as-synthesized nanoplates, along with the overall molar ratio of Ni to Cu of the products. As can be seen from Fig. 5, as the reaction temperature rose from 175 to 240 °C, the shape of the Ni–Cu bimetallic NCs changed from spherical to a shape with negative curvature edges which would grow into triangular and hexagonal nanoplates at a higher temperature (210–220 °C). When the reaction temperature reached 240 °C, once again, all of the NCs transformed into nanospheres which contained a higher weight percentage of Ni than the NCs synthesized at a low temperature such as 175 °C. In order to form highly anisotropic nanoplates, there needs to be a balance in the reduction rate of Ni(II) and the oxidative etching rate. In other words, the reduction must become substantially slow with the assistance of oxidative etching. When at a low temperature (e.g. 175 °C) the reduction of Ni(acac)₂ was relatively slow, and galvanic replacement reactions would take a dominant role, therefore a great deal of Ni atoms would be oxidatively etched back to the solution. As a result, only spherical nanoparticles with a diameter of about 20 nm were formed (Fig. 5a). Once the temperature increased to 190 °C, clover-like NCs could be generated (Fig. 5b). This might be induced by the strong oxidative etching effect of Cu(II) at a low reaction temperature. When the reaction temperature rose to 210 °C, some triangular nanoplates were formed by eliminating the {111} facets from the side surfaces (Fig. 5c). Further increasing



Scheme 1 Schematic illustration for the formation of triangular and hexagonal Ni–Cu alloy nanoplates.

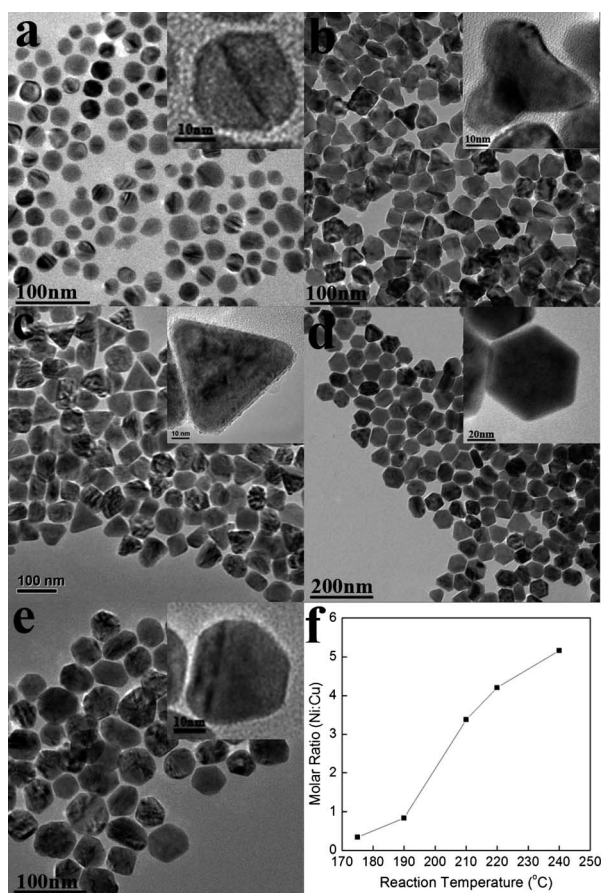


Fig. 5 TEM images of five as-synthesized samples illustrating the morphological evolution when reaction temperatures were applied at 175 °C (a), 190 °C (b), 210 °C (c), 220 °C (d), and 240 °C (e). The insets show the enlarged image of a single NC. (f) Molar ratio of Ni to Cu (determined from EDS analyses) of the five as-synthesized samples obtained at different temperatures. More information about the syntheses is available in Table S1 (see No. 1–4 and No. 6) in ESI†.

the temperature to 220 °C led to dominantly hexagonal nanoplates (Fig. 5d). However, when the reaction temperature reached 240 °C, Ni(II) was reduced by oleylamine to generate Ni(0) atoms at a sufficiently high rate, and the final product would have no choice but to exist in the form of thermodynamically favored near-spherical NCs (Fig. 5e). The change in the shape of Ni–Cu NCs always accompanies a change in the overall molar ratio of Ni to Cu, which was confirmed by EDS analyses shown in Fig. 5f. The Ni content in the Ni–Cu NCs increased as the reaction temperature rose from 175 to 240 °C.

Roles of TOP and dibenzyl ether

TOP, which can coordinate with Ni strongly, acts as surface capping agent in the reaction. It adsorbs on the Ni surface to control the growth rate of Ni NCs. Therefore, TOP is indispensable in keeping the growth of Ni–Cu NCs under kinetic control and achieving anisotropic shapes. If no TOP is added, the reaction will be too fast for nanoplates to form and will result in big nanospheres with a diameter of about 130 nm, along with some nanorods which have a diameter of 135 nm (see

Fig. S13 in ESI†). Meanwhile, because Cu(II) cannot be reduced by oleylamine in the presence of Cl ions at a relatively low temperature, the concentration of oleylamine plays a vital role in tailoring the reduction rate of Ni(II) and the oxidative etching rate of Cu(II). In this work, dibenzyl ether was used as a non-reducing solvent to dilute the concentration of oleylamine. When the mixture solution containing 7 mL of dibenzyl ether and 3 mL of oleylamine was used to react with 1 mmol of Ni(acac)₂ and 0.2 mmol of CuCl₂·2H₂O at 200 °C, only triangular nanoplates were produced. As in the diluted oleylamine solution, the reduction rate of Ni(II) was restricted, and Cu(II) had enough time to etch Ni(0) back to Ni(II) during the galvanic replacement reaction before being covered by Ni atoms reduced by oleylamine. Therefore, the shape of the NCs would be different from that of NCs synthesized in undiluted oleylamine.

Magnetic properties

Fig. 6 describes the temperature dependence of magnetization (*M*–*T* curves) measured at an applied field of 100 Oe. For the ZFC measurement curves, a maximum of magnetization is observed at a temperature of about 305 K for the triangular nanoplate sample, while that for hexagonal sample is at about 325 K. For nanoparticle assembly which is composed of single domain nanoparticles that have a uniaxial magnetic anisotropy and uniform particle sizes, the temperature (*T*_{max}) corresponding to such a maximum equals the blocking temperature (*T*_B) at which the thermal energy overcomes all energy barriers so that the magnetic moments are able to reorient under the applied magnetic field within the time scale of the magnetization measurement (typically 100 s). However, since the prepared nanoplate samples do not have a unitary size distribution and a uniaxial magnetic anisotropy, the shape of the peak corresponding to *T*_{max} in the ZFC curves may be broadened or changed. The small jumps which occurred at low temperature (<25 K) for both the samples may also be related to particles with different sizes.

It is observed that the ZFC/FC curves of the triangular nanoplates branch off at a higher temperature compared to the hexagonal nanoplates. The difference between the ZFC and FC curves can be explained by the presence of an energy barrier that has to be overcome for the magnetic field to change the orientation of the magnetic moments. Since the two nanoplate samples have a close composition and the same crystalline phase, there should be close magnetocrystalline anisotropy constants for each nanoplate. In this case, an extrinsic magnetic anisotropy that resulted from the shape-anisotropy of the nanoplates certainly plays an important role in the observed result. Considering the geometric differences, the symmetry of a triangle is lower than that of a hexagon. In addition, the triangular nanoplates have a smaller thickness and larger edge length than the hexagonal nanoplates, which further increases the shape-anisotropic effect. Therefore it is possible that the improved shape-anisotropic energy for triangular nanoplates may contribute to the higher divergence temperature of magnetization in the ZFC/FC measurements. A similar phenomenon was also noticed in Ni nanosheets which had a high divergence temperature in the ZFC/FC curves.^{11,12}

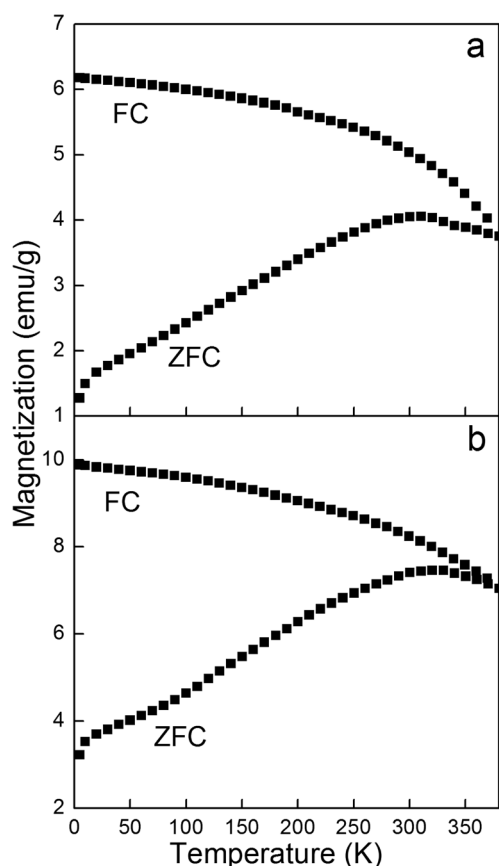


Fig. 6 ZFC and FC curves of the as-synthesized triangular (a) and hexagonal (b) Ni-Cu alloy nanoplates. The measuring field and cooling field are 100 Oe.

Fig. 7 shows the corresponding hysteresis loops of as-synthesized triangular (Fig. 7a) and hexagonal nanoplates (Fig. 7b) measured at two different temperatures. The coercivities are 200 and 10 Oe for the triangular nanoplates, and 30 and close to 0 Oe (in the limit range of SQUID measurement) for the hexagonal nanoplates at 5 and 300 K, respectively. These results indicate that it is easier for the hexagonal nanoplates to undergo the transition from the ferromagnetic to the superparamagnetic state upon increasing temperature, although the hexagonal nanoplates reveal a relatively higher T_{\max} compared to the triangular nanoplates. The observed larger coercivity of triangular nanoplates in comparison with that of hexagonal nanoplates may also be related to the shape-anisotropic effect. The measured saturated magnetizations (M_s) are 30 and 23 emu g^{-1} for the hexagonal nanoplates, and 21 and 16 emu g^{-1} for the triangular nanoplates at 5 and 300 K, respectively. The higher M_s values of the hexagonal nanoplates may correlate with the relatively higher content of Ni.

The magnetic behavior of Ni-Cu nanoplates can be tuned by controlling the amount of the metal precursors added which determines the final molar ratio of Ni to Cu. For example, the T_{\max} in the ZFC curve of hexagonal nanoplates that were synthesized with an equivalent molar ratio of Ni(acac)₂ and CuCl₂·2H₂O decreased to 190 K (see Fig. S14 in ESI†). Therefore it provides a convenient route to tune the magnetic

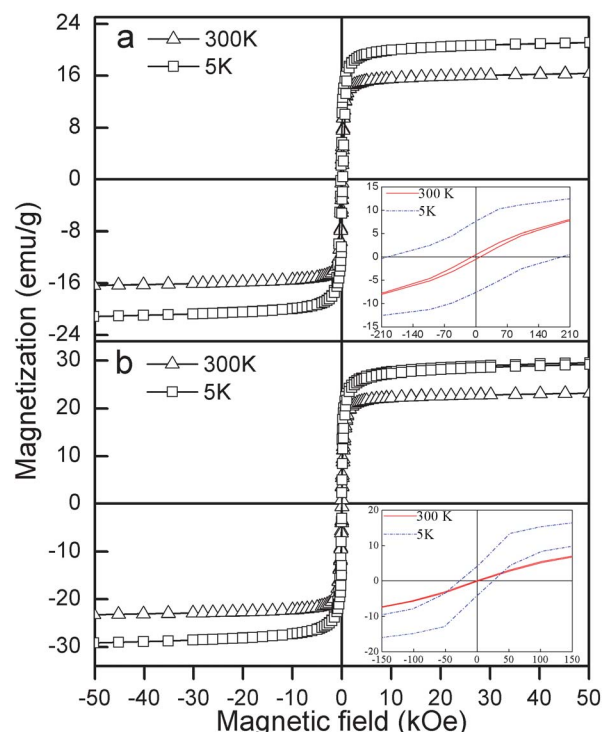


Fig. 7 Magnetic hysteresis loops of the as-synthesized triangular (a) and hexagonal (b) Ni-Cu alloy nanoplates. The insets show the low field detail of the magnetic hysteresis loops.

properties for different applications. For example, in the case of catalysis, suppose that the sample exhibits a superparamagnetic behaviour at room temperature, the magnetic interactions among nanoplates will be reduced by thermal energy. Therefore it will make the nanoplates more stable in the solutions and avoid agglomeration that may greatly reduce the catalytic efficiency. On the other hand, the highly saturated magnetization enables the nanoplates to be easily collected for recycling when an external magnetic field is applied.

Catalytic ability test

The catalytic performances of Ni-Cu alloy nanoplates were tested for the catalytic reduction of methylene blue by NaBH₄ in water. It is well-known that reduction of methylene blue by NaBH₄ in aqueous solution takes place very slowly without any catalysts but proceeds very rapidly in the presence of metallic catalysts, such as nickel nanoparticles.³⁷ The reaction process can be observed from the discolorization of methylene blue solution from deep blue to colorless after the addition of the catalysts (inset of Fig. 8). The catalytic reduction of methylene blue was monitored by UV-vis absorption spectroscopy of the reaction mixture after the addition of the catalysts. As can be seen in Fig. 8, the absorption spectrum of the mixture of methylene blue and sodium NaBH₄ displays a main peak at 664 nm, which disappears in one minute after the addition of hexagonal Ni-Cu alloy nanoplates (curve f in Fig. 8). This is because the double bond in the chromophore of methylene blue was broken by the addition of H₂ that was released through NaBH₄. The results also demonstrate that hexagonal nanoplates show slightly better

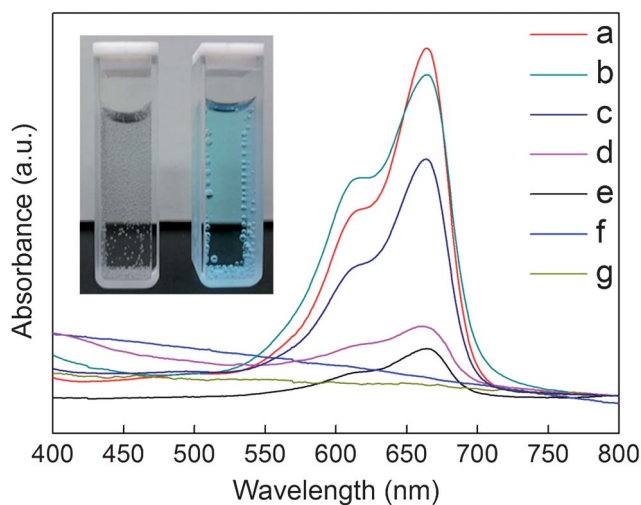


Fig. 8 UV-vis spectra of methylene blue aqueous solution in the presence of NaBH_4 . (a) Without any catalysts. (b) With added Cu nanoparticles after 120 min. (c) With added Ni nanoparticles after 5 min. (d) With added triangular Ni-Cu alloy nanoplates after 1 min. (e) With added Ni nanoparticles after 60 min. (f) With added hexagonal Ni-Cu alloy nanoplates after 1 min. (g) With added triangular Ni-Cu alloy nanoplates after 3 min. The inset shows the color change of methylene blue aqueous solution before (right) and after (left) adding hexagonal Ni-Cu alloy nanoplates.

catalytic ability than the triangular nanoplates. It should be noted that this reaction would not happen without the catalysis of Ni-Cu alloy nanoplates. For comparison, Ni nanoparticles with a mean diameter of 21 ± 1.4 nm (see Fig. S15 and S16 in ESI†) and Cu nanoparticles with a mean diameter of 28 ± 7.5 nm (see Fig. S17 and S18 in ESI†) which were synthesized by the decomposition of $\text{Ni}(\text{acac})_2$ or $\text{Cu}(\text{NO}_3)_2 \cdot 3\text{H}_2\text{O}$ in oleylamine solution (see ESI† for detailed synthetic methods) were chosen for testing. As a result, it took Ni nanoparticles more than one hour to achieve the degradation of methylene blue. There was still a small peak belonging to methylene blue that could be observed one hour after the addition of Ni nanoparticles. Cu nanoparticles showed almost no catalytic ability in this reaction. There was almost no change in the absorption spectrum of methylene blue.

The enhanced catalytic effect may be due to a couple of reasons. Firstly, nanoplates have higher surface-to-volume ratio than their spherical counterparts, therefore increasing the catalytic efficiency. In addition, atoms locating at the exposed edges and corners of the nanoplates may be more active than those on the surface of their spherical counterparts. Finally, the synergistic effects, such as electron transfer between Cu and Ni in the nanoplates, may enhance the catalytic performance. The as-prepared Ni-Cu alloy nanoplates may also be used as catalysts for other selectively heterogeneous reactions.

Conclusions

In summary, we demonstrate the synthesis of Ni-Cu alloy nanoplates through a facile one-pot route, in which the oxidative etching effect of $\text{Cu}(\text{II})$ in the presence of Cl^- ions plays a significant role. The as-synthesized nanoplates have an fcc crystalline

structure and exhibit two $\{111\}$ facets as the top and bottom faces, and a mixture of $\{100\}$ and $\{111\}$ facets as the side faces, although the $\{111\}$ side facets of triangular nanoplates tend to disappear. The forbidden $1/3\{422\}$ diffraction spots have been observed in the SAED pattern, indicating that crystalline defects offer a break to the cubic symmetry and could be important in the formation of the plate-like structure. By carefully adjusting the reduction rate of $\text{Ni}(\text{II})$ and the oxidative etching rate between $\text{Ni}(\text{0})$ and $\text{Cu}(\text{II})$, we can synthesize hexagonal or triangular Ni-Cu alloy nanoplates. The nanoplate compositions are correlated closely with the reaction temperatures. A high reaction temperature tends to generate nanoplates containing more Ni. The hexagonal nanoplates appear to undergo the transition from the ferromagnetic to the superparamagnetic state more easily upon increasing temperature compared to the triangular nanoplates. Larger coercivity and higher divergence temperature of magnetization in the ZFC/FC measurement have been observed in the triangular nanoplate sample. The magnetic properties of as-synthesized nanoplates can be readily tuned by adjusting the Ni content. In comparison with monometallic Ni and Cu nanoparticles, greatly enhanced catalytic performances have been observed for the catalytic reduction of methylene blue by NaBH_4 in aqueous solution by using the as-prepared Ni-Cu alloy nanoplates. We expect that the results presented herein may provide useful clues in the systematic study of shape control strategies and future applications of anisotropic magnetic metal NCs.

Acknowledgements

The authors gratefully acknowledge financial support from the National Outstanding Youth Science Foundation of China (Grant No. 50825101), the National Natural Science Foundation of China (Grant No. 50971108 and 51171158), and the Fundamental Research Funds for the Central Universities of China (Grant No. 201112G015).

Notes and references

- 1 Y. Liu and A. R. H. Walker, *Angew. Chem., Int. Ed.*, 2010, **49**, 6781.
- 2 W. Chen, R. Yu, L. Li, A. Wang, Q. Peng and Y. Li, *Angew. Chem. Int. Edit.*, 2010, **49**, 2917.
- 3 B. Lim, J. Wang, P. H. C. Camargo, C. M. Cobley, M. J. Kim and Y. Xia, *Angew. Chem., Int. Ed.*, 2009, **48**, 6304.
- 4 A.-X. Yin, X.-Q. Min, Y.-W. Zhang and C.-H. Yan, *J. Am. Chem. Soc.*, 2011, **133**, 3816.
- 5 Y. Tang and M. Ouyang, *Nat. Mater.*, 2007, **6**, 754.
- 6 B. Wiley, T. Herricks, Y. Sun and Y. Xia, *Nano Lett.*, 2004, **4**, 1733.
- 7 Y. Xiong, J. M. McLellan, J. Chen, Y. Yin, Z.-Y. Li and Y. Xia, *J. Am. Chem. Soc.*, 2005, **127**, 17118.
- 8 K. M. Bratlie, H. Lee, K. Komvopoulos, P. Yang and G. A. Somorjai, *Nano Lett.*, 2007, **7**, 3097.
- 9 C. Li, K. L. Shuford, Q. H. Park, W. Cai, Y. Li, E. J. Lee and S. O. Cho, *Angew. Chem.*, 2007, **119**, 3328.
- 10 V. F. Puentes, K. M. Krishnan and A. P. Alivisatos, *Science*, 2001, **291**, 2115.
- 11 Y. Leng, Y. Wang, X. Li, T. Liu and S. Takahashi, *Nanotechnology*, 2006, **17**, 4834.
- 12 Y. Leng, Y. Li, X. Li and S. Takahashi, *J. Phys. Chem. C*, 2007, **111**, 6630.
- 13 R. Xu, T. Xie, Y. Zhao and Y. Li, *Cryst. Growth Des.*, 2007, **7**, 1904.
- 14 D. S. Wang and Y. D. Li, *Adv. Mater.*, 2011, **23**, 1044.
- 15 J. Wu, J. Zhang, Z. Peng, S. Yang, F. T. Wagner and H. Yang, *J. Am. Chem. Soc.*, 2010, **132**, 4984.
- 16 Y. Lu, Y. Zhao, L. Yu, L. Dong, C. Shi, M.-J. Hu, Y.-J. Xu, L.-P. Wen and S.-H. Yu, *Adv. Mater.*, 2010, **22**, 1407.

-
- 17 S. Sun, C. B. Murray, D. Weller, L. Folks and A. Moser, *Science*, 2000, **287**, 1989.
- 18 Y. Zhang, W. Huang, S. E. Habas, J. N. Kuhn, M. E. Grass, Y. Yamada, P. Yang and G. A. Somorjai, *J. Phys. Chem. C*, 2008, **112**, 12092.
- 19 I. Robinson, S. Zacchini, L. D. Tung, S. Maenosono and N. T. K. Thanh, *Chem. Mater.*, 2009, **21**, 3021.
- 20 H. Guo, Y. Chen, X. Chen, R. Wen, G.-H. Yue and D.-L. Peng, *Nanotechnology*, 2011, **22**, 195604.
- 21 J.-M. Yan, X.-B. Zhang, T. Akita, M. Haruta and Q. Xu, *J. Am. Chem. Soc.*, 2010, **132**, 5326.
- 22 D. Wang and Y. Li, *J. Am. Chem. Soc.*, 2010, **132**, 6280.
- 23 A. I. Kirkland, D. A. Jefferson, D. G. Duff, P. P. Edwards, I. Gameson, B. F. G. Johnson and D. J. Smith, *Proc. R. Soc. London, Ser. A*, 1993, **440**, 589.
- 24 M.-P. Pileni, *Nat. Mater.*, 2003, **2**, 145.
- 25 V. Germain, J. Li, D. Ingert, Z. L. Wang and M. P. Pileni, *J. Phys. Chem. B*, 2003, **107**, 8717.
- 26 A. Courty, A. I. Henry, N. Goubet and M. P. Pileni, *Nat. Mater.*, 2007, **6**, 900.
- 27 R. Jin, Y. Cao, C. A. Mirkin, K. L. Kelly, G. C. Schatz and J. G. Zheng, *Science*, 2001, **294**, 1901.
- 28 N. N. Mallikarjuna and R. S. Varma, *Cryst. Growth Des.*, 2007, **7**, 686.
- 29 M. Tsuji, D. Yamaguchi, M. Matsunaga and M. J. Alam, *Cryst. Growth Des.*, 2010, **10**, 5129.
- 30 M. Tsuji, D. Yamaguchi, M. Matsunaga and K. Ikeda, *Cryst. Growth Des.*, 2011, **11**, 1995.
- 31 Z. L. Wang, *J. Phys. Chem. B*, 2000, **104**, 1153.
- 32 J. Zhang, M. R. Langille and C. A. Mirkin, *J. Am. Chem. Soc.*, 2010, **132**, 12502.
- 33 Y. Chen, D.-L. Peng, D. Lin and X. Luo, *Nanotechnology*, 2007, **18**, 505703.
- 34 F. Wetz, K. Soulantica, A. Falqui, M. Respaud, E. Snoeck and B. Chaudret, *Angew. Chem., Int. Ed.*, 2007, **46**, 7079.
- 35 H. Zhang, M. Jin, J. Wang, W. Li, P. H. C. Camargo, M. J. Kim, D. Yang, Z. Xie and Y. Xia, *J. Am. Chem. Soc.*, 2011, **133**, 6078.
- 36 Y. Sun, B. Mayers and Y. Xia, *Adv. Mater.*, 2003, **15**, 641.
- 37 W. Hao, T. Zhai, X. Wang and T. Wang, *Chem. J. Chinese Universities*, 2010, **31**, 1213.